Length-scale dependence of elastic strain from scattering measurements in metallic glasses

U. K. Vempati,[1] P. K. Valavala,[1,*] M. L. Falk,[2] J. Almer,[3] and T. C. Hufnagel[1,†]

[1]*Department of Materials Science and Engineering, Johns Hopkins University, Baltimore, Maryland 21218-2681, USA*

[2]*Department of Materials Science and Engineering, Department of Physics and Astronomy, and Department of Mechanical Engineering, Johns Hopkins University, Baltimore, Maryland 21218-2681, USA*

[3]*Advanced Photon Source, Argonne National Laboratory, Argonne, Illinois 60439, USA*

(Received 4 October 2011; revised manuscript received 18 May 2012; published 11 June 2012)

Several recent studies have reported that the elastic strain in metallic glasses, as measured from peak shifts in the pair-correlation functions of samples under load, increases with distance from an average atom, approaching the macroscopic strain at large distances. We have verified this behavior using high-energy x-ray scattering on metallic glasses loaded under uniaxial compression, uniaxial tension, and pure shear, and show that the apparent length-scale dependence of elastic strain is not an artifact of the assumption of structural isotropy in the data analysis. Molecular dynamics simulations of a binary Lennard-Jones glass loaded in uniaxial tension reproduce, qualitatively, the behavior observed in the experiments when the elastic strain is calculated from the shifts in the peaks of the pair-correlation function. Under hydrostatic loading, however, the length-scale dependence of elastic strain observed in the simulations is greatly reduced. This suggests that nonaffine atomic displacements, which are smaller under hydrostatic loading than under uniaxial loading, may play a key role in the length-scale dependence of elastic strain. Furthermore, no length-scale dependence is observed in simulations, for either uniaxial or hydrostatic loading, when the elastic strain is calculated from the average local deformation gradient tensor. We explain this apparent contradiction and show that the atomic displacements resulting from elastic loading are largest in the low-density regions between atomic shells around an average atom. Finally, we present an analysis of length-scale dependence of elastic strain calculated from the pair-correlation function for the case of homogeneous deformation, which is in good agreement with the simulations conducted under hydrostatic loading. For uniaxial loading, however, the analysis diverges from both the experimental and simulated results in the first two near-neighbor atomic shells. This suggests, in agreement with our observations from the molecular dynamics simulations, that the observed length-scale dependence of elastic strain from scattering measurements reflects the nature of the nonaffine atomic displacements in the glass.

DOI: 10.1103/PhysRevB.85.214201 PACS number(s): 81.05.Kf, 62.20.D−, 61.43.−j

I. INTRODUCTION

Several groups have recently reported measurements of elastic strain in metallic glasses under load using either x-ray or neutron scattering.[1–10] Calculating the elastic strain from shifts in the positions of peaks in the pair-correlation function $g(r)$, these groups observed that the elastic strain measured in this way increases with distance from an average atom (r), asymptotically approaching the macroscopically imposed strain. Given that elastic strain in either a crystal or an elastic continuum is expected to be independent of length scale, the question arises as to whether the observation of a length-scale-dependent elastic strain in metallic glasses might be an artifact of either the experiment or the data analysis. If it is not, it is natural to then inquire as to the nature of the physical mechanism responsible for this length-scale dependence.

In this paper, we describe a series of experimental and computational investigations into these issues. In Sec. II we present results from *in situ* x-ray scattering experiments on amorphous $Zr_{57}Ti_5Ni_8Al_{10}Cu_{20}$ under uniaxial tension, uniaxial compression, and pure shear loading. We show that the length-scale dependence of elastic strain from shifts in $g(r)$ peak positions is apparent in all three of these loading conditions. We also show that the length-scale dependence of elastic strain under uniaxial loading is not an artifact of assuming, in the analysis of the scattering data, that the structure is isotropic.

In Sec. III we present results from molecular dynamics simulations of a model binary Lennard-Jones glass that reproduce, on a qualitative basis, the nature of the length-scale dependence of elastic strain for uniaxial loading from shifts in the peak positions in $g(r)$. Models of hydrostatic loading, on the other hand, show essentially no length-scale dependence. A comparison of different algorithms for calculating the strains suggests that the observed length-scale dependence of strain is a consequence of the nature of nonaffine atomic displacements in the first few nearest-neighbor atomic shells around an average atom.

Finally, in Sec. IV we analyze the effect of a uniform elastic strain on the pair-correlation function $g(r)$ for the case of uniaxial and hydrostatic loading, which we then compare to our experimental and simulation results. For the case of hydrostatic loading, the agreement is good at all length scales, while there is significant disagreement in the first few atomic shells for the case of uniaxial loading. In agreement with our other results, this observation suggests that nonaffine displacements in uniaxial loading contribute to the observed length-scale dependence of elastic strain in the scattering experiments.

II. LENGTH-SCALE DEPENDENCE OF STRAIN FROM X-RAY SCATTERING EXPERIMENTS

A. Experimental techniques and data analysis

We prepared metallic glass plates of nominal composition $Zr_{57}Ti_5Ni_8Al_{10}Cu_{20}$ by an arc-melting and suction-casting procedure described in detail elsewhere.[11] For the uniaxial

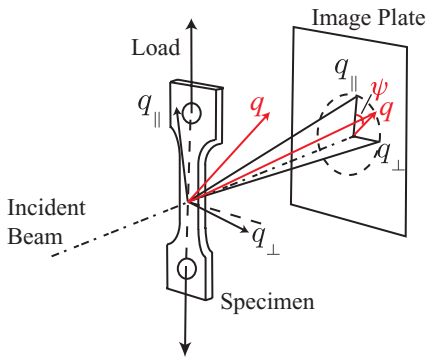

FIG. 1. (Color online) Experimental setup for the *in situ* x-ray scattering experiments, using the case of uniaxial tension as an example. $q_\parallel$ and $q_\perp$ are the scattering vectors approximately parallel and perpendicular to the loading direction, respectively. The azimuthal angle ψ is also shown; note that $q_\parallel$ corresponds to $\psi = 0^\circ$ and $q_\perp$ to $\psi = 90^\circ$ on the image plate.

tension experiments, we fabricated dog-bone tensile specimens (gage section 11.2 × 2.8 × 2.4 mm) by electrodischarge machining from suction-cast plates, removing the damaged surface layer by mechanical polishing to a final grit size of 25 μm. For the pure shear experiments, we employed an asymmetric four-point bend geometry using samples of overall dimensions 25 × 8 × 2.4 mm. In this geometry, loading via asymmetrically opposing pairs of pins produces a region of nominally pure shear strain in a region between two central notches in the plate. Reference 12 provides a complete discussion of the asymmetric four-point bend geometry.

We performed *in situ* high-energy x-ray scattering experiments on amorphous $Zr_{57}Ti_5Ni_8Al_{10}Cu_{20}$ under several loading conditions at beam line 1-ID of Advanced Photon Source. The data for samples under uniaxial compression are from our earlier work.[2] The scattering techniques and analysis for tension and pure shear experiments are largely the same as before, except as noted below. The tension and pure shear measurements were performed using 87 keV x-rays, with the x-ray scattering recorded in transmission through the specimen on a MAR 345 image plate positioned ~390 mm downstream from the sample (Fig. 1).

The samples were loaded in increments using a screw-driven MTS load frame, with pauses to record the scattering patterns. We converted the two-dimensional data from the image plate into 72 one-dimensional (intensity I vs scattering vector magnitude q) scattering patterns by dividing the image area into 5° wedges using the software package FIT2D.[13,14] Each of these patterns corresponds to a specific direction characterized by the azimuthal angle ψ around the incident beam direction, measured relative to the loading (vertical) direction (Fig. 1). We corrected the raw data for various effects, including absorption, multiple scattering, fluorescence, and polarization to obtain the scattered intensity $I(q,\psi)$ on an absolute scale. These intensity data were then normalized to obtain the direction-dependent total structure factor,

$$S(q,\psi) = \frac{I(q,\psi) - \langle f(q)f^*(q)\rangle}{\langle f(q)\rangle\langle f^*(q)\rangle}, \qquad (1)$$

where $f(q)$ is the atomic scattering factor and the angle brackets indicate averaging over the composition of the material.

B. Elastic strain from $g(r,\psi)$: Isotropic assumption

In analyzing scattering data from amorphous materials, it is usual to assume that the structure is isotropic. Although it is clear that uniaxial loading must introduce some anisotropy into the structure, in our prior work[2] we assumed that, for the small strains associated with elastic deformation, the induced anisotropy was negligible. Other workers have made the same assumption,[1,6,10] but it has been called into question on the basis of scattering experiments on specimens subjected to much larger homogeneous plastic strains, where the anisotropy is clearly not negligible.[15] In this section, we discuss data analysis under the isotropic assumption before moving on to the more rigorous spherical harmonic analysis in Sec. II C below.

Beginning with the assumption that the structure of the specimen is isotropic, we can calculate the pair-distribution function $\rho(r,\psi)$ by sine Fourier transformation of $S(q,\psi)$,

$$\rho(r,\psi) = \rho_\circ + \frac{1}{2\pi^2}\int_0^\infty S(q,\psi)\frac{\sin(qr)}{qr}q^2\,dq, \qquad (2)$$

where $\rho_\circ$ is the average atomic density of the glass. For consistency with our earlier work,[2] the results below are presented in terms of the pair-correlation function,

$$g(r,\psi) = \frac{\rho(r,\psi)}{\rho_\circ}.$$

Since the positions of the peaks in $g(r,\psi)$ give the distances of neighboring atomic shells relative to an average atom in the material, elastic strain can be measured from the shift in the peak position from the reference (undeformed) material to the deformed material under load. In practice we find it easiest and most reliable to measure this peak shift by a comparison of the positions at which $g(r,\psi) = 1$, as described in Ref. 2. Calling these positions $d(\sigma,r,\psi)$, we calculate the elastic strain $\epsilon(r,\psi)$ from

$$\epsilon(r,\psi) = \frac{d(\sigma,r,\psi)}{d(\sigma = 0,r,\psi)} - 1. \qquad (3)$$

From the direction-dependent elastic strains $\epsilon(r,\psi)$, we can determine the principal strains using the usual expression for transformation of strains,

$$\epsilon(r,\psi) = \epsilon_1(r)\cos^2\theta + \epsilon_2(r)\sin^2\theta, \qquad (4)$$

where θ is the angle between the laboratory coordinate system (Fig. 1) and the principal axes of strain, and $\epsilon_1(r)$ and $\epsilon_2(r)$ are the principal strains in the directions approximately parallel to and perpendicular to the loading axis. Fitting Eq. (4) to the measured $\epsilon(r,\psi)$ yields $\epsilon_1(r)$ and $\epsilon_2(r)$ as well as the rotation angle θ. For uniaxial tension and compression, $\theta \simeq 0$, and the elastic strains we report below are the principal strains $\epsilon_1(r)$ and $\epsilon_2(r)$. For pure shear, $\theta \simeq 45^\circ$, and we report below the shear strain $\gamma = |\epsilon_1(r) - \epsilon_2(r)|$.

Figure 2 shows elastic strain as a function of r, measured at several loads for each of the three loading geometries. In each case, we observe that the strain is smallest at small r (in the first nearest-neighbor shell) and increases with increasing r.

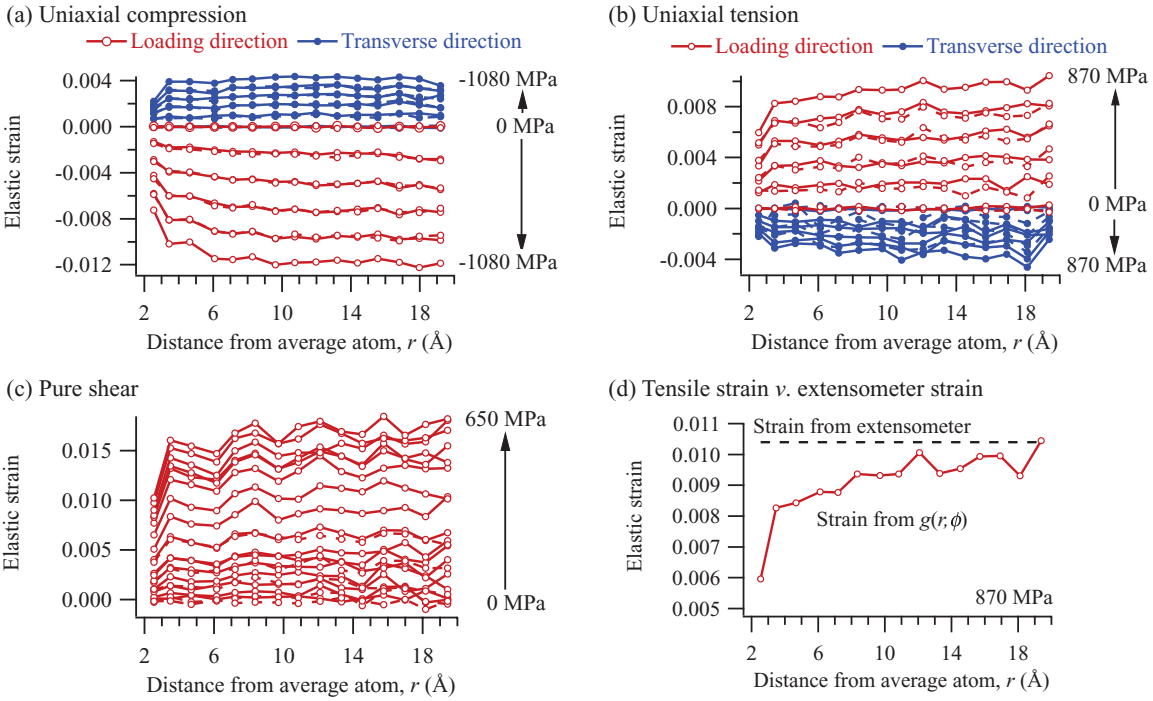

FIG. 2. (Color online) Elastic strain from $g(r,\psi)$ as a function of load and distance from average atom (r) for $Zr_{57}Ti_5Ni_8Al_{10}Cu_{20}$ specimens loaded in (a) uniaxial compression, (b) uniaxial tension, and (c) pure shear. Solid lines represent strain at a given stress during loading, while dashed lines are strain during unloading. (d) Tensile strain at a single load [870 MPa, from part (b)], along with the macroscopic strain recorded by an extensometer attached to the sample (dashed line). With increasing r, the elastic strain measured in the x-ray experiment asymptotically approaches the macroscopic strain.

In Fig. 2(d), we compare the elastic strain from the scattering experiment with that obtained simultaneously from an extensometer placed on the specimen. It is apparent that the x-ray strain is smallest in the first nearest-neighbor atomic shell, increasing with r to approach the macroscopic strain measured with the extensometer. These observations are consistent with earlier observations (by our group and others) on samples loaded in uniaxial compression[1,2] and tension.[5,7,10] Note that the data in Fig. 2(c) are reported for loading in pure shear.

C. Elastic strain from $g(\vec{r})$: Effect of anisotropy

Equation (2) assumes that the structure of the material is isotropic. In reality, mechanical deformation can make a metallic glass anisotropic, either irreversibly by plastic deformation[16] or, in the present case, reversibly by elastic deformation. This raises the possibility that the reported length-scale dependence of elastic strain is an artifact of the isotropic assumption. In particular, Dmowski and Egami showed, for a plastically deformed metallic glass, that the error introduced into $g(r,\psi)$ by making the isotropic assumption (compared to a fully anisotropic analysis) is largest at small r, just where we find the x-ray elastic strain to be most different from the macroscopic strain [Fig. 2(d)].[15] In this section we consider this possibility, and show that the length-scale dependence of elastic strain persists even under a fully anisotropic analysis.

To account for anisotropy, we expand the pair-distribution function into spherical harmonics,

$$\rho(\vec{r}) = \sum_{n,m} \rho_n^m(r) Y_n^m(\phi,\theta), \tag{5}$$

where $Y_n^m(\phi,\theta)$ are the spherical harmonics; ϕ and θ are the polar and azimuthal angles, respectively (Fig. 3); and $n = 0,1,2,\ldots$ and $m = -l,\ldots,l$ are, respectively, polar and azimuthal indices on $Y_n^m(\phi,\theta)$.[17] The spherical harmonics $Y_n^m(\phi,\theta)$ are given by

$$Y_n^m(\phi,\theta) = (-1)^m \sqrt{\frac{(2n+1)}{4\pi}\frac{(n-m)!}{(n+m)!}} P_n^m(\cos\phi) e^{im\theta}, \tag{6}$$

where P_n^m are the associated Legendre functions.[17] For uniaxial loading, we assume that the structure is transversely isotropic (i.e., isotropic in the x-y plane), which allows us to drop the dependence on the azimuthal angle θ and consider only harmonics with $m = 0$. The spherical harmonics then reduce to

$$Y_n(\phi) = \sqrt{\frac{(2n+1)}{4\pi}} P_n(\cos\phi) \tag{7}$$

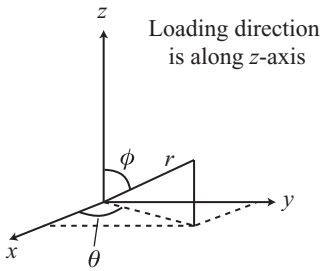

FIG. 3. Spherical coordinate convention used in this paper. The loading direction is along the z axis.

and the anisotropic pair-distribution function becomes

$$\rho(\vec{r}) = \rho(r,\phi) = \sum_n \rho_n(r) Y_n(\phi). \quad (8)$$

To extract the anisotropic pair-distribution function from the scattering data, we also expand the structure factor into spherical harmonic terms,

$$S(\vec{q}) = S(q,\phi) = \sum_n S_n(q) Y_n(\phi), \quad (9)$$

where ϕ is the polar angle (Fig. 3). Because we have scattering information over a range of ψ (directly related to ϕ), we can determine the individual harmonic terms $S_n(q)$ from $S(q,\phi)$ using the orthogonality relationship[18–20]

$$S_n(q) = C_n \int_0^{\pi/2} S(q,\phi) P_n(\cos\phi) \sin(\phi)\, d\phi, \quad (10)$$

where $n = 0,2,4,\ldots$ and $C_n = \sqrt{4\pi(2n+1)}$.

The first two terms in the structure factor, $S_0(q)$ and $S_2(q)$, are shown in Fig. 4 for a sample under zero load, and under a large compressive load (−1080 MPa, approximately 60% of the yield stress). As expected for a nominally isotropic specimen, $S_2(q)$ is found to be near zero for the unloaded specimen. Even for the specimen under load, $S_2(q)$ is much smaller in magnitude than $S_0(q)$. We note, however, that the relative magnitudes of $S_0(q)$ and $S_2(q)$ for elastic loading are comparable to those for plastically deformed glasses,[15] indicating that elastic loading does in fact induce significant structural anisotropy.

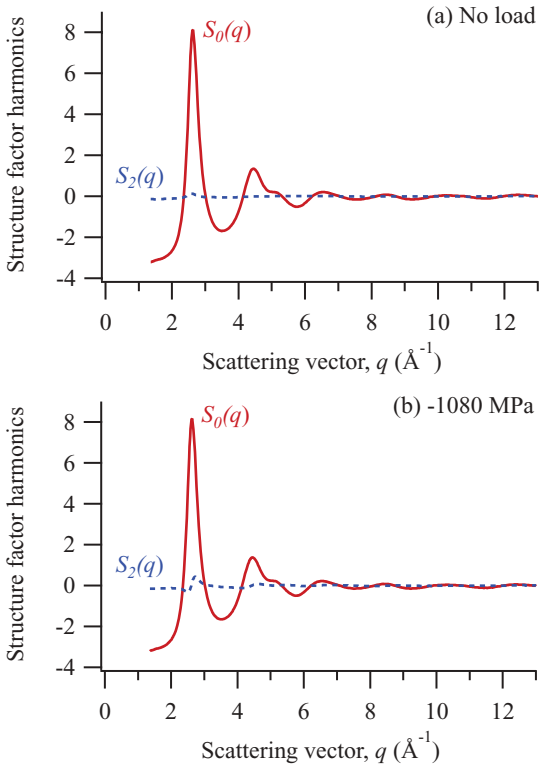

FIG. 4. (Color online) First two harmonics of the structure factor, $S_0(q)$ and $S_2(q)$, when the sample is (a) unloaded and (b) under 1080 MPa compressive load.

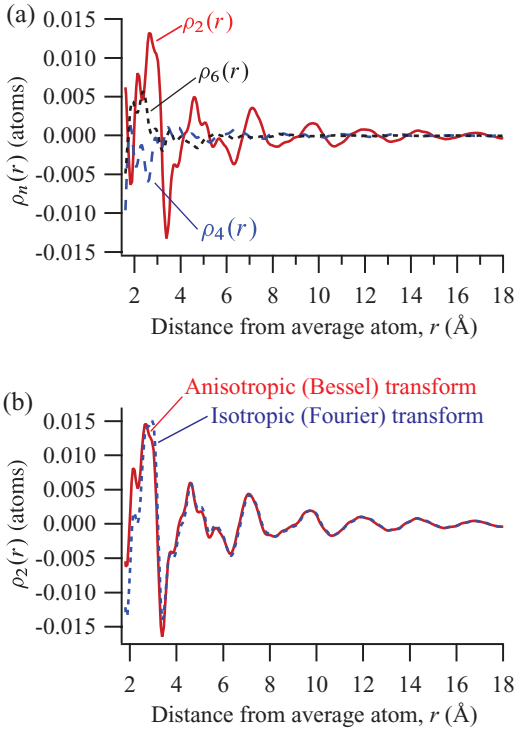

FIG. 5. (Color online) (a) Pair-distribution function harmonics $\rho_n(r)$ obtained from $S_n(q)$ using Eq. (11). (b) The second harmonic, $\rho_2(r)$, obtained by transformation of $S_2(q)$ using the spherical Bessel transform, given by Eq. (11), and the sine Fourier transform, given by Eq. (2).

To investigate the degree of anisotropy induced by elastic deformation in real space, and its effect on strain measurements, we calculate the harmonics of the pair-distribution function from the structure factor harmonics using the Bessel transformation,

$$\rho_n(r) = \frac{(\sqrt{-1})^n}{2\pi^2} \int_0^\infty S_n(q) J_n(qr) q^2\, dq, \quad (11)$$

where $J_n(qr)$ is the nth-order spherical Bessel function.[21] The first term $[\rho_0(r)]$ is isotropic, with information about any structural anisotropy residing in the higher-order ($n = 2,4,\ldots$) terms. Figure 5(a) shows the first few terms in $\rho_n(r)$, of which the $n = 2$ term is the largest. To identify the effect of this anisotropy on the analysis, we obtain two versions of $\rho_2(r)$ by transformation of $S_2(q)$, one using the isotropic assumption [Eq. (2)] and one using the anisotropic form [Eq. (11)].[15] The results are presented in Fig. 5(b). The magnitude of the discrepancy is largest at low r, just where the length-scale dependence of elastic strain is most significant [Fig. 2(d)].

To examine the possibility that the length-scale dependence of elastic strain in Fig. 2 is due to this discrepancy, we determined the elastic strain using a full anisotropic analysis. We calculated $\rho_n(r)$ for $n = 0$, 2 from $S_n(q)$ using Eq. (11) and $\rho(r,\phi)$ and $g(r,\phi)$ using Eq. (8). From peak shifts in $g(r,\phi)$, we determined the principal strains, using the same methods described in the previous section. The results are shown in Fig. 6 for three conditions (no load, −440 MPa, and −1080 MPa), along with the elastic-strain values obtained using the isotropic assumption. The agreement in elastic strain between

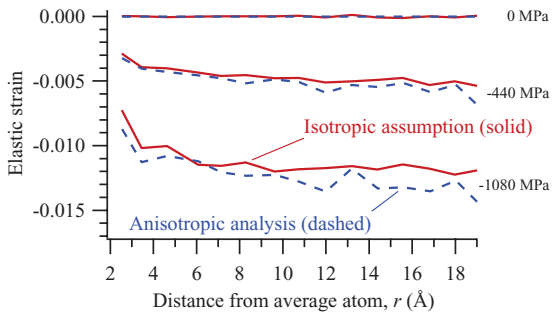

FIG. 6. (Color online) Elastic strain in the loading direction measured from the pair-correlation functions obtained using the isotropic transformation, given by Eq. (2), and the anisotropic transformation, given by Eq. (11). Data are for $Zr_{57}Ti_5Ni_8Al_{10}Cu_{20}$ loaded in uniaxial compression.

the isotropic assumption and the full anisotropic analysis is good at all values of r. (Some deviations in the elastic-strain data are observed, particularly at large compressive loads; however, these do not appear systematically different from the elastic strain calculated by isotropic analysis.) Most significantly, the trend for decreasing strain at small r is apparent in both cases. Mattern and coworkers, also using an anisotropic analysis, reached a similar conclusion in their experiments on Cu-Zr glasses.[5] We conclude that although uniaxial elastic loading does introduce a measurable structural anisotropy, the observed length-scale dependence of elastic strain persists whether the data are analyzed using the isotropic assumption or with a full anisotropic treatment.

III. MOLECULAR DYNAMICS SIMULATIONS

The results above show that the length-scale dependence of elastic strain in metallic glasses is not a result of the isotropic assumption in calculating $g(r,\psi)$. To confirm this observation and gain additional insight into the underlying physical mechanisms, we carried out molecular dynamics simulations on a model binary Lennard-Jones glass. Although too simple to capture all of the behavior of real metallic glasses, Lennard-Jones glasses provide a starting point for exploration. For this reason, they are commonly used in computational studies of amorphous alloys.[22–26]

A. System details

The general form of the Lennard-Jones potential is

$$U_{\alpha\beta}(r) = 4\epsilon_{\alpha\beta}\left[\left(\frac{\sigma_{\alpha\beta}}{r}\right)^{12} - \left(\frac{\sigma_{\alpha\beta}}{r}\right)^{6}\right], \qquad (12)$$

where α and β are indices specifying the atom kinds, $\epsilon_{\alpha\beta}$ is the interaction energy, and $\sigma_{\alpha\beta}$ is the distance at which attractive and repulsive terms cancel. Our specific model system is a Wahnstrom glass,[27] with equal numbers of two kinds of atoms (denoted A and B) and parameters $\epsilon_{AA} = \epsilon_{BB} = \epsilon_{AB} = 1.0$, $\sigma_{AA} = 1.0$, $\sigma_{BB} = 5/6$, and $\sigma_{AB} = \sigma_{BA} = 11/12$. The mass of the species A (m_A) is twice that of species B (m_B). (Our choice of this parametrization was motivated by the fact that it has been employed extensively in the research community for simulating metallic glasses.)[26] The potential was shifted such that any interactions above a cutoff distance $r_c = 2.5\sigma_{AA}$ may be neglected. Additional details of the system studied can be found elsewhere.[28] To describe physical quantities in the simulation, we use reduced Lennard-Jones (LJ) units and choose ϵ_{AA}, σ_{AA}, and m_B as the normalizing terms for energy, length, and mass, respectively. The temperature is given in units of ϵ/k_B (where k_B is Boltzmann's constant), pressure is given in ϵ/σ^3, and distance is given in σ.[29] A characteristic relaxation time $\tau = \sigma_{AA}\sqrt{m/\epsilon_{AA}}$ is used to describe the time scale of the simulations.

TABLE I. Three-stage quench schedule for the binary Lennard-Jones glass.

Stage	T_{initial} (ϵ/k)	T_{final} (ϵ/k)	P_{initial} (ϵ/σ^3)	P_{final} (ϵ/σ^3)	Duration (τ)
1	1.2	0.73	13.3	7.98	250
2	0.73	0.45	7.98	4.73	10 000
3	0.45	0.036	4.73	0.0	250

We conducted our simulations using LAMMPS[30,31] code on an initially cubic box with dimensions $45\sigma \times 45\sigma \times 45\sigma$. Initially, 116 640 atoms were placed in the box randomly, followed by relaxation to minimize potential energy to eliminate atomic overlaps. After equilibration in the liquid state ($T_{\text{initial}} = 1.2$, $P_{\text{initial}} = 13.3$) for 750τ, the glass was quenched to a final temperature $T_{\text{final}} = 0.036$ and pressure $P_{\text{final}} = 0.0$ following the three-stage quench schedule shown in Table I. The second stage of the quench is longest, during which the system goes through the mode coupling temperature ($T = 0.57$) (Ref. 28) over a time period of $10\,000\tau$. A Nose-Hoover[32] thermostat and a Parrinello-Rahman barostat[33,34] were used to control the system temperature and pressure, respectively.

As described in detail below, we subjected our model glass to several loading conditions and used several techniques to study the length-scale dependence of the resulting elastic strain. To calculate the elastic strains, we averaged the atomic positions over a time of 500τ to minimize the effect of thermal displacements. We determined the imposed normal elastic strain ϵ_i from the change in size of the simulation box:

$$\epsilon_i = \frac{L_i^{\text{def}} - L_i^{\text{ref}}}{L_i^{\text{ref}}}, \qquad (13)$$

where L_i^{ref} and L_i^{def} are the box sizes along direction $i = x,y,z$ before and after deformation, respectively. This imposed elastic strain is analogous to the macroscopic elastic strain measured by extensometer in our experiments, and we use it as a basis of comparison for the length-scale dependence of the atomistic-level elastic strains calculated from the simulations.

B. Uniaxial deformation

Our first simulations were intended to provide the most direct comparison possible to the experimental results (within the limitations of the simple model system). We therefore subjected the model glass to uniaxial tensile deformation by decreasing the pressure along the z axis from $P_z = 0$ to $P_z = -0.5$ using an N-P-T ensemble. This load was chosen to give a 1% elastic strain along the loading direction. During the loading, the temperature of the system was maintained at

$T = 0.036$, and the pressure on the lateral faces of the box was maintained at $P_x = P_y = 0$. In the transverse direction, the system was found to contract due to the Poisson effect.

1. Elastic strain from the pair-correlation function, $g(\vec{r})$

The primary motivation in constructing this model was to compare elastic strain calculated based on the pair-correlation function from the model with that determined from the experiments. As in the experiment, we assume transverse isotropy, reducing $g(\vec{r})$ to $g(r,\phi)$ by averaging over the azimuthal angle θ. (The spherical coordinate convention in Fig. 3 applies here as well.) The angle-dependent pair-correlation function is then

$$g(r,\phi) = \frac{V}{N^2 \times dV} \left\langle \sum_i \sum_{j \neq i} \delta(r - r_{ij})|_{(\phi)_{ij}=\phi} \right\rangle, \quad (14)$$

where V is the volume of the simulation box, dV is the volume of a spherical shell of radius r and thickness dr, and i and j are indices which run over all of the N atoms in the system.[35] We calculated elastic strain from $g(r,\phi)$ by the same $\sin^2\phi$ analysis used for the experimental data.

The elastic strain determined from the uniaxial tension simulations using the $g(r,\phi)$ technique is shown in Fig. 7, along with the imposed strain determined from the change in simulation box length using Eq. (13). (The figure also shows strain calculated in two other ways, which are discussed below.) We observe a length-scale dependence of the elastic strain similar to that observed in the experiments, with a strain that is smallest in the first near-neighbor shell and which increases with r. The convergence to the imposed strain is, however, rather slower than that we observe in the experiment. This may be the result of the small simulation size, which creates significant uncertainty in $g(r,\phi)$ for $r > 3\sigma$ and necessitates using a cone of larger half-angle to calculate $g(r)$ (18° here compared to 2.5° for the experiments).

Uncertainty at large r aside, the length-scale dependence of elastic strain from $g(r,\phi)$ in the simulation is strikingly similar to that obtained from the scattering experiments. Because the simulations involve calculation of the pair-correlation function

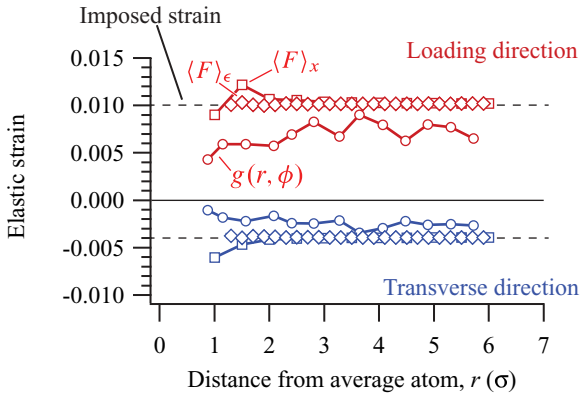

FIG. 7. (Color online) Elastic strain in the model glass subject to uniaxial tension, at $T = 0.036$, calculated using three different techniques: shifts in pair-correlation function $g(r,\phi)$ peaks; the deformation gradient tensor, averaging local strains $\langle F \rangle_\epsilon$; and the deformation gradient tensor, averaging atomic positions $\langle F \rangle_x$. The imposed strain calculated using Eq. (13) is also shown.

directly from the atomic positions, they are not subject to the question of which transform to apply (isotropic Fourier sine vs anisotropic spherical Bessel). Together with the results of Sec. II C, this allows us to state unequivocally that the observed length-scale dependence of elastic strain is not an artifact of an assumption of isotropy in analyzing the experimental data.

2. Elastic strain from the local deformation gradient

To gain additional insight into the nature of the length-scale dependence of elastic strain, we also calculated the elastic strain in our simulated systems with a more sophisticated methodology that involves calculation of the local strain tensor around each atom.[24,36] For each atom, we identify the neighboring atoms that are within a distance r of the central atom in the reference (i.e., undeformed) configuration. In the deformed configuration, each of these neighbors will have experienced a displacement relative to the central atom. We can then determine the local strain tensor corresponding to the deformation gradient tensor F that produces the best fit (in a least-squares sense) with the actual atomic displacements determined from the model. Once the local strain tensor for each atom is known, the global average strain tensor is readily calculated. By varying the distance r over which neighbors are identified, we can use this approach to explore the length-scale dependence of elastic strain.

The elastic strain determined in this way from our uniaxial tension simulations is shown in Fig. 7. Because three neighbors are required to uniquely determine the deformation gradient,[36] the elastic strain using this algorithm is indeterminate for $r < \sigma$. But it is apparent that the elastic strain calculated from the deformation gradient agrees well with the imposed strain for $r > 2\sigma$, and in particular that there is no significant length-scale dependence in the first several atomic shells around the average atom.

Why is there such a striking difference between the elastic strains calculated from $g(r,\phi)$ and those calculated using the deformation gradient approach? One difference is that while both methods involve averaging over all of the atoms, the order in which the averaging is done is different. In determining elastic strain from $g(r,\phi)$, we first determine an average atomic environment, and from changes in that average structure, we determine an average strain. In the deformation gradient approach, however, we determine the elastic strain for each atom first, and then average the strains.

To determine whether the order of averaging influences the elastic-strain calculation from the model, we adapted the deformation gradient approach to work on a global average structure. Starting from a reference atom, we discretized the model into bins of size $dr \times d\theta \times d\phi$. The separations between the reference atom and all other atoms in the undeformed configuration were calculated and stored in the (r, θ, ϕ) bin corresponding to that pair. This process was then repeated, using each atom in turn as the reference atom. The distances stored in each bin were averaged to produce a structure that represents the atomic environment around an average atom in the material. To this point, the procedure is similar to how $g(r,\phi)$ is calculated. But here, in the case of the *deformed* configuration, we repeat the pair-separation calculation for a given bin for the *same* atomic pairs that

contributed to that bin in the undeformed configuration. This is different from the $g(r,\phi)$ calculation, where the atomic pairs contributing to a given bin in reference and deformed configurations may be different.

Having determined the average structure in this way, making sure that the same atom pairs were counted in both configurations, we determined the best-fit strain tensor describing the deformation necessary to transform the reference configuration to the deformed configuration. The approach is basically the same as the deformation gradient approach described above, except that here we average the environments first and then calculate the elastic strain, instead of calculating the local elastic strains first and then averaging them.

The result of this calculation is also shown in Fig. 7. Except for the first few points (at small r), the agreement with the original deformation gradient technique is good. This makes it clear that the order of averaging has a minor influence on the elastic strain calculated using the deformation gradient approach, and can be ruled out as a source of the length-scale dependence of elastic strain obtained from the pair-correlation function.

3. *Elastic strain from atomic shells*

Besides the order of averaging, there are other differences when the strain is extracted from $g(r)$ compared to the deformation gradient technique. For example, in the pair-correlation approach, the volume of atoms examined is essentially a thin shell of thickness dr at a distance r from an average atom; changes in the population of atoms at particular values of r are interpreted in terms of a strain, according to Eq. (3). In the deformation gradient approach, all of the atoms in a reference sphere of radius r are considered.

A possibly more subtle difference is the lack of a precise reference in the pair-correlation technique. When calculating elastic strain from peak shifts in $g(r,\phi)$ [Eq. (3)], it is implicitly assumed that the atomic pairs in the undeformed and deformed states are the same, and that the change in their separations is reflected in the movement of peaks in $g(r,\phi)$ due to changes in bond lengths. But this is not necessarily true. Atomic pairs from neighboring volume elements can move in and out of an element of interest, complicating the calculation of the elastic strain. We expect that this will be an especially important effect if the material experiences nonaffine atomic rearrangements in response to the imposed strain. Indeed, Table II shows that about 6% of the atoms in the simulations of uniaxial deformation experience at least one change in their Voronoi near-neighbor environments, as compared to about 2.6% for simulations of hydrostatic deformation (discussed in Sec. III C below). The uncertainty as to which atoms are contributing to the measured strain from $g(r,\phi)$ is in contrast to the deformation gradient approach, where the displacements of specific atoms (those initially in the reference volume) are considered, and only these displacements are used in the strain calculation.

To examine the influence of these effects, we developed an approach that combines the volume discretization and averaging behavior of the $g(r,\phi)$ method with the use of a precise reference as in the deformation gradient method. In this hybrid approach, we tabulate the separations between a reference atom and all of its neighbors within a shell of radius r and thickness dr. By repeating this process using every atom in the system in turn as the reference, we obtain a table of pair separations in this shell for an average atom in the material. For the undeformed configuration, these shells are nominally spherical, with radii R_x, R_y, and R_z determined by a least-squares fit to the neighbor separations. We then repeat this procedure for the deformed configuration; in general, the nominally spherical reference volumes are deformed into ellipsoids (for uniaxial loading) with best-fit radii r_x, r_y, and r_z. Although similar to a pair-correlation calculation, this approach differs in that the same atoms chosen from the reference spherical shell are used to calculate the shape of the ellipsoidal shell in the deformed state. If x, y, and z are the principal axes, the principal strains are then given by

$$\epsilon_i = \frac{r_i - R_i}{R_i}, \tag{15}$$

where $i = x,y,z$. Because of the shape of the shells in the deformed configuration, we refer to this method as the "ellipsoid fit." As with the deformation gradient method, we can probe the length-scale dependence of the elastic strain determined in this way by varying R_i.

The results of this approach are shown in Fig. 8, along with the elastic-strain values obtained from $g(r,\phi)$ and the deformation gradient. Interestingly, the elastic strain calculated by the ellipsoid-fit method shows different behavior from either the pair-correlation or deformation gradient approaches. The elastic strain oscillates about the imposed strain, with the difference being largest for small values of r. This observation is discussed in detail in Sec. V.

C. Hydrostatic deformation

The considerations described above suggest that the length-scale dependence of elastic strain from $g(r,\phi)$ is related to

TABLE II. Changes in Voronoi near-neighbor atomic environments for various loading conditions, from molecular dynamics simulations at $T = 0.036$. The table entries are the fraction of atoms that have the specified number of neighboring atoms that are different between the reference (unloaded) atomic configuration and the configuration under load.

Number of different neighbors between reference and deformed states	Uniaxial tension ($\epsilon = 0.0102$)	Uniaxial compression ($\epsilon = -0.0093$)	Hydrostatic tension ($\epsilon = 0.0078$)
0	0.9311	0.9361	0.9724
1	0.0645	0.0597	0.0264
2	0.0039	0.0038	0.0011
3 or more	0.0005	0.0005	0.0001

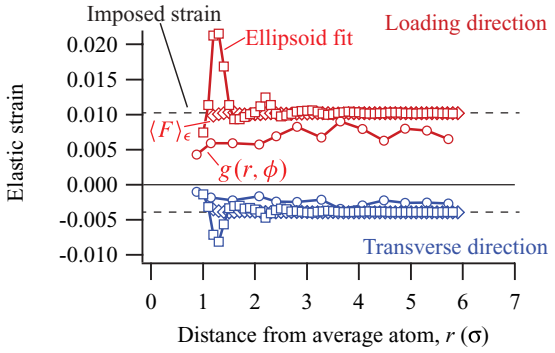

FIG. 8. (Color online) Elastic strain in the model glass subject to uniaxial tension calculated using the ellipsoid-fit method, along with the strain calculated from peak shifts in the pair-correlation function $[g(r,\phi)]$, the deformation gradient tensor ($\langle F \rangle_\epsilon$), and the imposed strain.

nonaffine atomic displacements that occur in response to loading. To examine this possibility, we conducted simulations in which the model was subjected to hydrostatic tension. Under hydrostatic loading, there is no global shear strain, although nonaffine displacements can still arise due to local shear strains in the disordered glass structure. We speculated, therefore, that the length-scale dependence of elastic strain from $g(r,\phi)$ would be smaller for hydrostatic loading than for uniaxial loading.

To verify this speculation, we simulated hydrostatic tension on our binary Lennard-Jones glass and calculated the elastic strain using the techniques described above. The results are shown in Fig. 9. It is apparent that the length-scale dependence of elastic strain from the $g(r,\phi)$ approach is much weaker, and the calculated strain at large r matches the macroscopically imposed strain (compare Fig. 7). This suggests that the apparent length-scale dependence of elastic strain is in fact related to nonaffine atomic rearrangements, and hence strongly influenced by the presence of a shear component of strain. We believe that the shear strain drives the exchanges of atomic neighbors that underlie the apparent length-scale dependence of elastic strain calculated from $g(r,\phi)$.

The results of using the ellipsoid-fit technique for calculating strain under hydrostatic loading are also shown in Fig. 9.

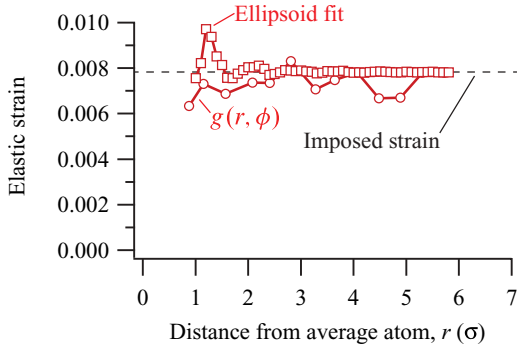

FIG. 9. (Color online) Elastic strain in the model glass subject to hydrostatic tension calculated using the ellipsoid-fit method, along with the strain calculated from peak shifts in the pair-correlation function $[g(r,\phi)]$ and the imposed strain. Note the difference in scale compared to Fig. 8.

Although there are fluctuations similar to those for uniaxial loading (Fig. 8), they are much smaller than in the uniaxial case and they damp out more quickly with increasing r. We discuss this behavior in more detail in Sec. V below.

D. Characteristics of nonaffine displacements

If the observed length-scale dependence of strain from $g(r)$ is related to nonaffine atomic displacements, then it becomes of interest to analyze the nature of the nonaffine displacements under various loading conditions. One important aspect of the nonaffine displacements, discussed above, is that they can result in changes in the identities of the atomic near neighbors around a given atom (Table II). Here we briefly consider other aspects of the nonaffine displacements in both uniaxial and hydrostatic loading.

Given that our simulations employed a simple Lennard-Jones potential, we believe that there is little to be gained from a close analysis of specific atomic-scale structures and rearrangements (e.g., in terms of atomic clusters). However, the models do show distinctive qualitative features that depend on the loading condition. Figure 10 shows quiver plots of the nonaffine displacements from the simulations of (a) uniaxial tension and (b) hydrostatic tension. It is immediately apparent that the nonaffine displacements are not homogeneously distributed, but instead are concentrated in regions spanning several atomic diameters, indicating that the elastic deformation is inhomogeneous on this length scale. As one might expect, the magnitude of the nonaffine displacements is smaller for hydrostatic loading than for uniaxial loading [Fig. 10(c)], and while the nonaffine displacements are isotropically distributed for hydrostatic loading, under uniaxial loading they are preferentially oriented along the loading axis [Fig. 10(d)].

We note that other researchers have suggested that elastic deformation in amorphous materials could be nonuniform. For example, in three-dimensional (3D) Lennard-Jones simulations of elastic deformation of a polydisperse glass, Leonforte and coworkers observed nonuniform nonaffine atomic displacements and measured a correlation length of $\sim 23\sigma$.[37] More recently, Dmowski and coworkers suggested, from x-ray scattering data, that only about three-quarters of the atoms in a metallic glass deform elastically, with the remainder being anelastic "liquidlike" material.[38]

IV. ANALYSIS OF VARIATIONS IN $g(r)$ DUE TO NONUNIFORM DEFORMATION

We offer here an additional analysis of our data and simulations that suggests that deformation in the first few atomic shells is, in fact, inhomogeneous. To do so, we will derive conditions on the values of $g(r)$ for the reference (undeformed) and deformed configurations that should hold if the deformation were homogeneous, and show that these conditions are violated for both the experimental data and the results from the simulations in the case of uniaxial deformation.

To carry out this analysis, we first write the pair-correlation function in Cartesian coordinates. If the pair-correlation function of a glass in the reference configuration is $g^{\text{ref}}(\vec{r})$,

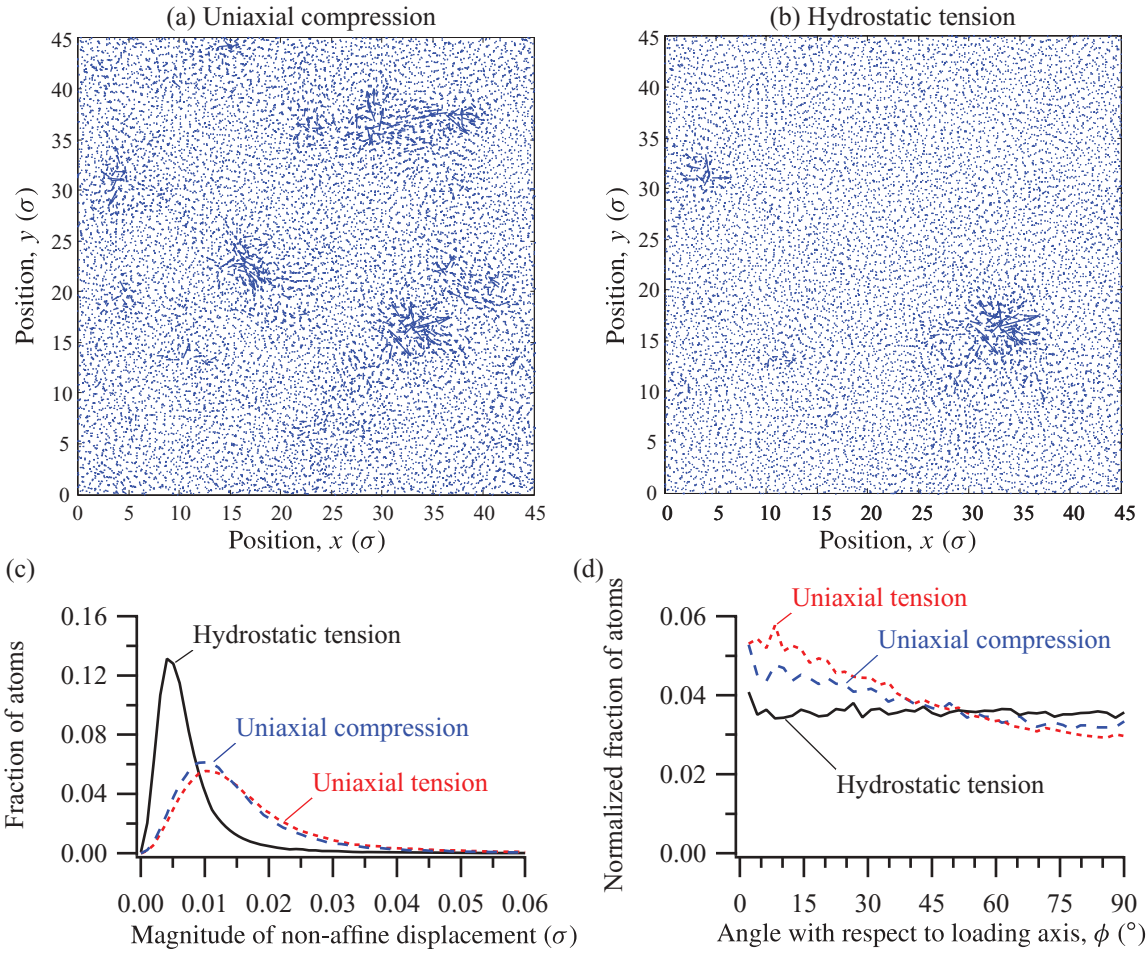

FIG. 10. (Color online) Nonaffine displacements in the simulations of elastic deformation. Slices through atomic configurations subjected to (a) uniaxial compression and (b) hydrostatic tension show the nonaffine displacements projected onto the x-y plane (perpendicular to the loading axis, z). The lengths of the arrows indicating the nonaffine displacements have been multiplied by a factor of 20. In (c) and (d), we show the distributions of the magnitudes and orientations, respectively, of the nonaffine displacements. In (d), the histogram is normalized by a geometrical factor of $(\sin\phi)^{-1}$.

then in the Cartesian system,

$$g^{\rm ref}(\vec{r}) = g^{\rm ref}(x,y,z),$$

where "ref" stands for reference and x,y,z are the Cartesian coordinates. If the glass is subjected to deformation described by the elastic-strain tensor,

$$\boldsymbol{\epsilon} = \begin{pmatrix} \epsilon_x & 0 & 0 \\ 0 & \epsilon_y & 0 \\ 0 & 0 & \epsilon_z \end{pmatrix},$$

then the pair-correlation function in the deformed state can be written as[39]

$$g^{\rm def}(x,y,z) = g^{\rm ref}\left(\frac{x}{1+\epsilon_x}, \frac{y}{1+\epsilon_y}, \frac{z}{1+\epsilon_z}\right). \quad (16)$$

Expanding the term on the right-hand side of above equation into Taylor series, we have (neglecting higher-order terms)

$$g^{\rm def}(x,y,z) = g^{\rm ref}(x,y,z) - \left(x\epsilon_x\frac{\partial}{\partial x} + y\epsilon_y\frac{\partial}{\partial y} + z\epsilon_z\frac{\partial}{\partial z}\right) \times g^{\rm ref}(x,y,z). \quad (17)$$

This equation is valid only when the strains (ϵ_x, ϵ_y, and ϵ_z) are small and uniform throughout the sample.

Equation (17) can be simplified in certain special cases. For example, when an isotropic material is subject to uniaxial deformation, the strain tensor can be written as

$$\boldsymbol{\epsilon} = \begin{pmatrix} -\nu\epsilon & 0 & 0 \\ 0 & -\nu\epsilon & 0 \\ 0 & 0 & \epsilon \end{pmatrix},$$

where ν is Poisson's ratio. Then, Eq. (17) becomes (now switching to spherical coordinate notation)

$$g^{\rm def}(r,\phi) - g^{\rm ref}(r) = -r\epsilon(\cos^2\phi - \nu\sin^2\phi)\frac{d}{dr}[g^{\rm ref}(r)]. \quad (18)$$

[Note that in the above equation, r in $g^{\rm ref}(r)$ is a scalar signifying the fact that the pair-correlation function of an amorphous material in an undeformed configuration is assumed to be spherically symmetric. Also for this reason, the derivative is a full derivative and does not depend upon θ or ϕ.] If our assumptions of small, uniform deformation of an isotropic

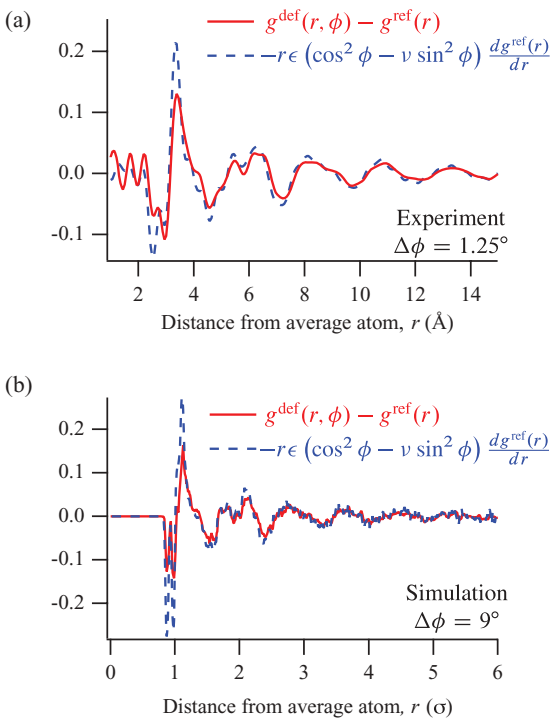

FIG. 11. (Color online) Left-hand and right-hand sides of Eq. (18) obtained from (a) experimental and (b) simulation data in uniaxial tension. Solid curves depict the difference between pair-correlation functions in deformed $[g^{\mathrm{def}}(r,\phi)]$ and reference $[g^{\mathrm{ref}}(r)]$ states, i.e., the left-hand term of Eq. (18), of (a) $Zr_{57}Ti_5Ni_8Al_{10}Cu_{20}$ specimen and (b) model glass. In both cases, deformation is due to a tensile load applied along the z axis; thus, the polar angle $\phi = 0°$ corresponds to the loading direction. Pair-correlation functions were calculated by averaging over an angular range of ψ, or equivalently, $\phi = 2.5°$ in the case of the *in situ* experiments and $\phi = 18°$ in the case of the simulated system. Dashed curves depict the expected $g^{\mathrm{def}}(r,\phi) - g^{\mathrm{ref}}(r)$ given by the right-hand side of Eq. (18).

material hold, then the two sides of Eq. (18) should be equal for all values of r. These are plotted in Fig. 11 for experiment as well as simulation data obtained during uniaxial tensile deformation. In both cases, we see good agreement between the two sides of Eq. (18) at large r, but significant disagreement at small r, particularly in the first two neighbor shells. The fact that Eq. (18) does not hold in either case (at small r) leads us to believe that elastic deformation is inhomogeneous in glasses subject to uniaxial loading.

As a check on this conclusion, we can examine the results for the simulations conducted under hydrostatic deformation. We modify Eq. (18) to reflect the conditions of hydrostatic deformation,

$$g^{\mathrm{def}}(r) - g^{\mathrm{ref}}(r) = -r\epsilon\frac{d}{dr}g^{\mathrm{ref}}(r), \tag{19}$$

where $\epsilon = \Delta/3$ and Δ is the dilatation due to the applied hydrostatic tension. Hydrostatic deformation is isotropic and hence the pair-correlation function of the deformed glass is only dependent on r. Figure 12 shows the two sides of Eq. (19). We see that the agreement is rather good over the entire range of r. We conclude that the assumptions underlying Eq. (19) are valid for the case of hydrostatic deformation.

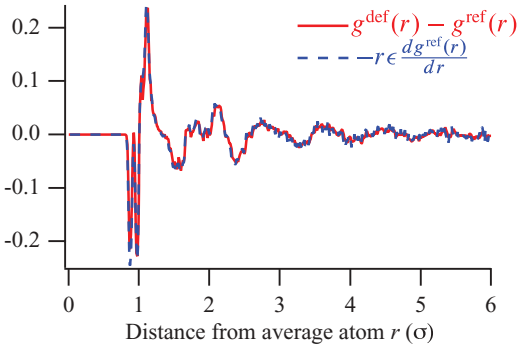

FIG. 12. (Color online) Left-hand and right-hand terms in Eq. (19) are shown here, as solid and dashed curves, respectively, for the simulated system subject to hydrostatic tension. Note that ϵ here represents $\Delta/3$, where Δ is the dilatation induced by the imposed stress. Also note that the pair-correlation function in the deformed configuration is isotropic, hence terms involving θ or ϕ do not appear, unlike the case of uniaxial deformation (Fig. 11).

This observation corroborates our view that inhomogeneity of elastic deformation of a metallic glass is most pronounced in the presence of a resolved shear stress, and that this inhomogeneity in strain leads to the observed length-scale dependence of elastic strain from $g(r,\phi)$ in the first few atomic near-neighbor shells.

V. DISCUSSION

Additional insight into the microscopic elastic-strain response (and the nonaffine displacements) of the model system subject to uniaxial tension can be gained by comparing the elastic strain calculated using the ellipsoid-fit technique with the pair-correlation function. In Fig. 13, the elastic strain in the loading direction calculated by the ellipsoid-fit technique is plotted along with $g(r)$ from the reference system. It can be seen that the peaks in elastic strain calculated using the ellipsoid-fit technique occur at positions in r corresponding to minima in $g(r)$. In other words, the largest strains are at values of r where the atomic density is lowest; correspondingly, the smallest strains are within the atomic shells themselves.

Some caution is necessary in interpreting this observation because most of the atoms occur in the atomic shells [i.e.,

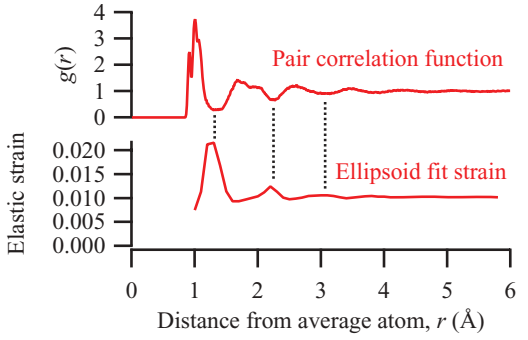

FIG. 13. (Color online) Elastic strain in the loading direction in the model glass subject to uniaxial tension calculated using the ellipsoid-fit method (bottom) along with the pair-correlation function $g(r)$ (top).

the peaks in $g(r)$] with relatively few atoms between shells (in the valleys). Still, it suggests that the compliance of the structure is greatest in the region between shells. Recently, Ma and coworkers reached a similar conclusion on the basis of an analysis of reciprocal-space [$S(q)$] experimental data.[40] Their interpretation of their observations invoked strongly bonded (and therefore stiff) solute-centered clusters, with relatively weaker and less-stiff bonding between clusters.

One might readily expect a decrease in modulus, and hence an increase in elastic strain, with increasing separation between atoms. Elastic modulii can be related to the curvature of the potential-energy–pair-separation relationship in solids.[41] At the equilibrium pair separation [corresponding to the first peak in $g(r)$], the curvature is large and the modulus is high. Atomic pairs at larger separations, however, interact more weakly and have a lower modulus. These more compliant regions would deform more in response to an applied stress, resulting in the behavior shown in Fig. 13. As discussed above, the deformation gradient approach to calculating elastic strain is less sensitive to this effect because it considers entire volumes, and not atomic shells.

The precise manner in which this kind of heterogeneous deformation manifests itself as a length-scale dependence of elastic strain calculated from the pair-correlation function is not entirely clear. As noted in our prior work,[2] the different stiffness of different kinds of bonds probably plays a role in the first near-neighbor shell. Also, as pointed out above, the choice of atoms differs between the ellipsoid fit and $g(r)$ calculations; it may be that this lack of a precise reference is responsible for the length-scale dependence.

On a different note, the agreement among different algorithms at large values of r (Fig. 8) corroborates our view of the origin of length-scale dependence of strain. Based on the behavior of elastic strain calculated using the ellipsoid-fit method, it appears that the effect of heterogeneous deformation or nonaffine displacements is significant within about three or four atomic distances from an average atom. This is apparent both from the simulations (Fig. 8) and the experiments (Fig. 2). That such a length-scale exists has been pointed out by many researchers in various classes of disordered materials.[42–45] This characteristic length may very well have important implications for both elastic and plastic deformation of metallic glasses. In particular, it may be related to the size of shear transformation zones (the fundamental units of plastic deformation in metallic glasses), which are thought to contain about 20 to 100 atoms corresponding to a diameter of about 4 to 6 Å.[46] Further investigations are necessary to establish the validity and physical significance of these length scales.

VI. CONCLUSIONS

We tested amorphous $Zr_{57}Ti_5Ni_8Al_{10}Cu_{20}$ specimens *in situ* under uniaxial tension, uniaxial compression, and pure shear loading and found that elastic strain determined from position shifts in pair-correlation function $g(r,\phi)$ in all three cases is dependent on r. The elastic strain calculated from the angle-dependent $g(r,\phi)$ of a model binary Lennard-Jones glass subject to uniaxial tension reproduces, qualitatively, the length-scale dependence observed in the experiments. In contrast, virtually no length-scale dependence was observed for a model glass subjected to hydrostatic loading. A comparison of three different methods of calculating strain on the atomic scale suggests that the source of the length-scale dependence of elastic strain (measured from the pair-correlation functions) is related to the presence of heterogeneous nonaffine atomic displacements. A simple analysis shows that the assumption of homogeneous deformation is valid at large r (for both simulations and experiments), but that this assumption breaks down in the first few atomic shells. In particular, the strain is inhomogeneous due to high compliance in the regions between atomic shells, where the atomic density is low.

ACKNOWLEDGMENTS

We thank Jonathan Trenkle and Noël Walker for their help with data collection, and Gabe Morris for his help with machining the specimens. We would like to acknowledge helpful discussions with Stephan Hruszkewycz, K. T. Ramesh, and Robert Cammarata. This work was funded by the National Science Foundation (NSF) under Grants No. DMR-0307009 and No. DMR-0705517. Participation of M.L.F. in this work was supported by funds from the NSF under Grant No. DMR-0808704. Use of the Advanced Photon Source, an Office of Science User Facility operated for the US Department of Energy (DOE) Office of Science by Argonne National Laboratory, was supported by the US DOE under Contract No. DE-AC02-06CH11357.

*Present address: Advanced Materials Laboratory, Department of Mechanical Engineering, Northwestern University, 2145 Sheridan Road, Evanston, Illinois 60202, USA.

†hufnagel@jhu.edu

[1] H. Poulsen, J. Wert, J. Neuefeind, V. Honkimaki, and M. Daymond, Nature Mater. **4**, 33 (2005).

[2] T. C. Hufnagel, R. T. Ott, and J. Almer, Phys. Rev. B **73**, 064204 (2006).

[3] M. Stoica, J. Das, J. Bednarcik, G. Wang, G. Vaughan, W. H. Wang, and J. Eckert, JOM **62**, 76 (2010).

[4] S. Sato, H. Suzuki, T. Shobu, M. Imafuku, Y. Tsuchiya, K. Wagatsuma, H. Kato, A. D. Setyawan, and J. Saida, Mater. Trans. **51**, 1381 (2010).

[5] N. Mattern, J. Bednarcik, S. Pauly, G. Wang, J. Das, and J. Eckert, Acta Mater. **57**, 4133 (2009).

[6] X. D. Wang, J. Bednarcik, H. Franz, H. B. Lou, Z. H. He, Q. P. Cao, and J. Z. Jiang, Appl. Phys. Lett. **94**, 011911 (2009).

[7] M. Stoica, J. Das, J. Bednarcik, H. Franz, N. Mattern, W. H. Wang, and J. Eckert, J. Appl. Phys. **104**, 013522 (2008).

[8] T. Wilson, B. Clausen, T. Proffen, J. Elle, and D. Brown, Metall. Mater. Trans. A **39A**, 1942 (2008).

[9] J. Das, M. Bostrom, N. Mattern, A. Kvick, A. R. Yavari, A. L. Greer, and J. Eckert, Phys. Rev. B **76**, 092203 (2007).

[10] X. D. Wang, J. Bednarcik, K. Saksl, H. Franz, Q. P. Cao, and J. Z. Jiang, Appl. Phys. Lett. **91**, 081913 (2007).

[11]X. Gu, L. Xing, and T. Hufnagel, J. Non-Cryst. Solids **311**, 77 (2002).
[12]O. Ünal, I. E. Anderson, J. L. Harringa, R. L. Terpstra, B. Cook, and J. Foley, J. Electron. Mater. **30**, 1206 (2001).
[13]A. P. Hammersley, ESRF Internal Report No. ESRF97HA02T, 1997 (unpublished).
[14]A. Hammersley, S. Svensson, M. Hanfland, A. Fitch, and D. Hausermann, High-Pressure Res. **14**, 235 (1996).
[15]W. Dmowski and T. Egami, J. Mater. Res. **22**, 412 (2007).
[16]F. O. Mear, G. Vaughan, A. R. Yavari, and A. L. Greer, Philos. Mag. Lett. **88**, 757 (2008).
[17]G. Arfken, *Mathematical Methods for Physicists* (Academic, Orlando, FL, 1985).
[18]M. E. Milberg, J. Appl. Phys. **33**, 1766 (1962).
[19]M. J. Regan, Ph.D. thesis, Stanford University, 1993.
[20]M. J. Regan and A. Bienenstock, J. Phys. IV **3**, 459 (1993).
[21]N. Norman and B. E. Warren, J. Appl. Phys. **22**, 483 (1951).
[22]D. Deng, A. S. Argon, and S. Yip, Philos. Trans. Roy. Soc. A **329**, 549 (1989).
[23]D. Srolovitz, V. Vitek, and T. Egami, Acta Metall. Mater. **31**, 335 (1983).
[24]M. L. Falk and J. S. Langer, Phys. Rev. E **57**, 7192 (1998).
[25]M. Tsamados, A. Tanguy, C. Goldenberg, and J.-L. Barrat, Phys. Rev. E **80**, 026112 (2009).
[26]M. L. Falk and C. E. Maloney, Eur. Phys. J. B **75**, 405 (2010).
[27]G. Wahnstrom, Phys. Rev. A **44**, 3752 (1991).
[28]Y. F. Shi and M. L. Falk, Phys. Rev. B **73**, 214201 (2006).
[29]See the documentation section of Ref. 31.
[30]S. Plimpton, J. Comput. Phys. **117**, 1 (1995).
[31][http://lammps.sandia.gov].
[32]W. G. Hoover, Phys. Rev. A **31**, 1695 (1985).
[33]M. Parrinello and A. Rahman, J. Appl. Phys. **52**, 7182 (1981).
[34]M. Parrinello and A. Rahman, J. Chem. Phys. **76**, 2662 (1982).
[35]Adaption of Eq. (2.94) in M. P. Allen and D. J. Tildesley, *Computer Simulation of Liquids* (Oxford University Press, New York, 1988).
[36]J. A. Zimmerman, D. J. Bammann, and H. Gao, Int. J. Solids Struct. **46**, 238 (2009).
[37]F. Leonforte, R. Boissiere, A. Tanguy, J. P. Wittmer, and J. L. Barrat, Phys. Rev. B **72**, 224206 (2005).
[38]W. Dmowski, T. Iwashita, C.-P. Chuang, J. Almer, and T. Egami, Phys. Rev. Lett. **105**, 205502 (2010).
[39] See Eq. (A3) in the appendix in Ref. 47.
[40]D. Ma, A. D. Stoica, X. L. Wang, Z. P. Lu, B. Clausen, and D. W. Brown, Phys. Rev. Lett. **108**, 085501 (2012).
[41]M. Born and K. Huang, *Dynamical Theory of Crystal Lattices* (Oxford University Press, New York, 1988).
[42]F. Leonforte, A. Tanguy, J. P. Wittmer, and J. L. Barrat, Phys. Rev. Lett. **97**, 055501 (2006).
[43]C. Maloney and A. Lemaitre, Phys. Rev. Lett. **93**, 195501 (2004).
[44]A. Tanguy, J. P. Wittmer, F. Leonforte, and J. L. Barrat, Phys. Rev. B **66**, 174205 (2002).
[45]I. Goldhirsch and C. Goldenberg, Eur. Phys. J. E **9**, 245 (2002).
[46]C. Schuh, T. Hufnagel, and U. Ramamurty, Acta Mater. **55**, 4067 (2007).
[47]D. Weaire, M. F. Ashby, J. Logan, and M. J. Weins, Acta Metall. Mater. **19**, 779 (1971).